European Radiology (2019) 29:2017–2026
https://doi.org/10.1007/s00330-018-5735-1

MAGNETIC RESONANCE

Quantitative susceptibility mapping in the human fetus to measure blood oxygenation in the superior sagittal sinus

Brijesh Kumar Yadav[1,2] · Sagar Buch[3] · Uday Krishnamurthy[1,2] · Pavan Jella[1] · Edgar Hernandez-Andrade[4,5] · Anabela Trifan[1] · Lami Yeo[4,5] · Sonia S. Hassan[4,5,6] · E. Mark Haacke[1,2] · Roberto Romero[4,7,8,9] · Jaladhar Neelavalli[1,10]

Received: 12 February 2018 / Revised: 12 August 2018 / Accepted: 28 August 2018 / Published online: 1 October 2018

Abstract

Objectives To present the feasibility of performing quantitative susceptibility mapping (QSM) in the human fetus to evaluate the oxygenation (S_vO_2) of cerebral venous blood in vivo.

Methods Susceptibility weighted imaging (SWI) data were acquired from healthy pregnant subjects (n = 21, median = 31.3 weeks, interquartile range = 8.8 weeks). The susceptibility maps were generated from the SWI-phase images using a modified QSM processing pipeline, optimised for fetal applications. The processing pipeline is as follows: (1) mild high-pass filtering followed by quadratic fitting of the phase images to eliminate background phase variations; (2) manual creation of a fetal brain mask that includes the superior sagittal sinus (SSS); (3) inverse filtering of the resultant masked phase images using a truncated k-space approach with geometric constraint. Further, the magnetic susceptibility, $\Delta\chi_v$ and corresponding putative S_vO_2 of the SSS were quantified from the generated susceptibility maps. Systematic error in the measured S_vO_2 due to the modified pipeline was also studied through simulations.

Results Simulations showed that the systematic error in S_vO_2 when using a mask that includes a minimum of 5 voxels around the SSS and five slices remains < 3% for different orientations of the vessel relative to the main magnetic field. The average $\Delta\chi_v$ in the SSS quantified across all gestations was 0.42 ± 0.03 ppm. Based on $\Delta\chi_v$, the average putative S_vO_2 in the SSS across all fetuses was 67% ± 7%, which is in good agreement with published studies.

Conclusions This in vivo study demonstrates the feasibility of using QSM in the human fetal brain to estimate $\Delta\chi_v$ and S_vO_2.

Key Points

- *A modified quantitative susceptibility mapping (QSM) processing pipeline is tested and presented for the human fetus.*
- *QSM is feasible in the human fetus for measuring magnetic susceptibility and oxygenation of venous blood in vivo.*
- *Blood magnetic susceptibility values from MR susceptometry and QSM agree with each other in the human fetus.*

Keywords Magnetic resonance imaging · Brain · Second trimester

✉ Roberto Romero
prbchiefstaff@med.wayne.edu

✉ Jaladhar Neelavalli
jneelava@med.wayne.edu

[1] Department of Radiology, Wayne State University School of Medicine, Detroit, MI, USA

[2] Department of Biomedical Engineering, Wayne State University College of Engineering, Detroit, MI, USA

[3] The MRI Institute for Biomedical Research, Waterloo, Ontario, Canada

[4] Perinatology Research Branch, NICHD/NIH/DHHS, Bethesda, Maryland and Detroit, MI, USA

[5] Department of Obstetrics and Gynecology, Wayne State University School of Medicine, Detroit, MI, USA

[6] Department of Physiology, Wayne State University School of Medicine, Detroit, MI, USA

[7] Department of Obstetrics and Gynecology, University of Michigan, Ann Arbor, MI, USA

[8] Department of Epidemiology and Biostatistics, Michigan State University, East Lansing, MI, USA

[9] Center for Molecular Medicine and Genetics, Wayne State University, Detroit, MI, USA

[10] Philips Innovation Campus, Philips India Ltd., Bengaluru, India

Abbreviations

$\Delta\chi_v$	Magnetic susceptibility
$\Delta\chi_{do}$	Magnetic susceptibility difference between fully oxygenated and deoxygenated fetal blood
BET	Brain Extraction Tool
BW	Bandwidth
dHb	Deoxyhaemoglobin
GA	Gestational age
Hct	Haematocrit
QSM	Quantitative susceptibility mapping
S_vO_2	Venous oxygen saturation
SAR	Specific absorption rate
SSS	Superior sagittal sinus
TH	Slice thickness

Introduction

Adequate oxygen supply to the fetus is an essential component of its normal growth and development [1]. Obstruction of this supply may lead to acute or chronic fetal hypoxia. This can be one of the major consequences of a compromised placental function, resulting from increased placental vascular resistance, preeclampsia, or an inflammatory condition [2–4]. An inadequate fetal response to hypoxia could render the fetal brain susceptible to injury [5, 6]. Indeed, chronic hypoxia is known to be a predictor of abnormal neurodevelopment and cognitive disabilities [7]. Therefore, the fetal cerebral blood oxygenation status could be an important physiological parameter in identifying fetuses at risk of brain injury. It is also an important quantity in understanding oxygen metabolism in the developing fetal brain in healthy homeostatic conditions.

Magnetic resonance imaging (MRI) is playing an increasingly important role in fetal diagnostic care. The ability to measure physiologic parameters, e.g. tissue metabolic status using MR spectroscopy (MRS) [8], volumetric blood perfusion using phase-contrast MRI [9], or blood oxygenation status using inherent tissue properties [10], has made MRI an important tool in quantitative fetal evaluation. MRS has the ability to detect and quantify the concentration of metabolites such as lactate, which is a downstream measure of tissue hypoxia [8]. Nevertheless, the ability to measure blood oxygen saturation would provide a direct measure of tissue hypoxia. Recent quantitative MRI-based works have used either the transverse relaxation rate property, T2, of blood [11] or the paramagnetic nature of deoxyhaemoglobin (dHb) with MR susceptometry [10, 12] to measure blood oxygenation status in vivo in the human fetus. Although the former method was successfully applied in the major vessels of the heart in third-trimester fetuses [11], it is susceptible to radiofrequency (RF) field inhomogeneities and is also associated with a high specific absorption rate (SAR), especially when imaging at 3.0 T [13]. On the other hand, MR susceptometry measures the magnetic susceptibility ($\Delta\chi$) of blood that, in turn, is related to the amount of dHb present. It uses the phase signal from a spoiled gradient-echo (GRE) MRI sequence for performing this measurement, which is associated with a low SAR, even at 3.0 T [14]. This method was recently applied in second- and third-trimester human fetuses to evaluate blood oxygenation (S_vO_2) in the superior sagittal sinus (SSS) [10]. One of the challenges of the model-based susceptometry method, however, is that it uses only the intravascular phase and assumes that the vessel has no/minimal curvature with a circular cross-section, which is not true in all cases. Furthermore, it requires knowledge of the orientation of the vessel relative to the main magnetic field, which can be difficult to ascertain in the presence of vessel curvature.

Quantitative susceptibility mapping (QSM), on the other hand, uses both the intravascular and extravascular phase to estimate the $\Delta\chi$ on a pixel-by-pixel basis. QSM is independent of the orientation and the shape/size of the structure of interest. Due to its ability to provide a direct measurement of the underlying spatial distribution of $\Delta\chi$ across different tissues [15], it has been used to measure S_vO_2 in the cerebral veins [16] and to detect haemorrhages or micro-bleeds [17]. QSM has also been used to diagnose hypoxic events and evaluate treatment efficacy in adults, children, and neonates [15, 18–22]. Although QSM holds tremendous potential to quantify blood S_vO_2 non-invasively, it has not been translated to fetal imaging applications yet.

Hence, the goal of this study is to evaluate an optimised QSM processing pipeline for the quantification of the susceptibility of the fetal cerebral vessels. We also report the first application of QSM to quantify the putative fetal cerebral S_vO_2. Given that fetal structures are small and that the surrounding environment is unique compared to adult imaging, the modified QSM processing pipeline was first evaluated using a digital phantom for possible systematic errors in quantifying $\Delta\chi_v$ and putative S_vO_2.

Materials and methods

Theory of QSM

Phase [$\varphi(r)$] data provide a direct measure of the field perturbation, $\Delta B(r)$ within a tissue relative to its immediate background. They are related by:

$$\varphi(r) = \gamma \cdot \Delta B(r) \cdot TE \quad (1)$$

where γ is the gyromagnetic ratio and TE is the echo time. For biological materials with $\chi \ll 1$, spatial susceptibility distribution and the corresponding $\Delta B(r)$ in the magnetising field B_0 can be related as follows [23]:

$$\Delta B(r) = FT^{-1}\left[FT[\Delta\chi(r)]\cdot\frac{1}{3}-\frac{k_z^2}{k_x^2+k_y^2+k_z^2}\right]\cdot B_0 \quad (2)$$

where $\Delta\chi(r)$ is the magnetic susceptibility distribution, FT is Fourier transform and k_x, k_y and k_z are the coordinates in the spatial frequency domain, commonly referred to as k-space. Using Eqs. 1 and 2, the measured $\varphi(r)$ in a tissue and the underlying $\Delta\chi(r)$ property are related as:

$$\varphi(r) = \gamma\cdot FT^{-1}\left[FT[\Delta\chi(r)]\cdot\frac{1}{3}-\frac{k_z^2}{k_x^2+k_y^2+k_z^2}\right]\cdot B_0\cdot TE \quad (3)$$

Thanks to the paramagnetic nature of dHb, the $\Delta\chi$ of venous blood is related to its oxygenation state via Eq. 4 [24]:

$$\Delta\chi_v = \Delta\chi_{do}.(1-S_vO_2).Hct \quad (4)$$

where $\Delta\chi_{do}$ represents the magnetic susceptibility difference between fully deoxygenated and fully oxygenated blood and Hct is the fractional hematocrit.

Re-writing Eq. 3 for $\Delta\chi(r)$:

$$\Delta\chi(r) = FT^{-1}\left(FT\left(\frac{\Delta\varphi(r)}{(\gamma.B_o.TE)}\right)\cdot\frac{1}{\frac{1}{3}-\frac{k_z^2}{k_x^2+k_y^2+k_z^2}}\right) \quad (5)$$

Equation 5 is the basis of the QSM approach that has been widely used to quantify in vivo blood oxygenation [16, 25–29].

Patient recruitment

Twenty-one women in their second (n = 5) and third trimester (n = 16) of pregnancy, who received routine obstetrical care at Hutzel Women's Hospital, Detroit, Michigan, USA, were non-consecutively recruited in this study. The median and interquartile range (IQR) of gestational age (GA) of the fetuses included were 31.3 weeks and 8.8 weeks, respectively. MRI scanning was approved by the local institutional review board (IRB) and was compliant with HIPAA regulations. Participants with a singleton, uncomplicated pregnancy with normal ultrasound examinations [10] and reporting no contraindications for MRI were eligible. Written informed consent was obtained before the MRI scan. Fetal SWI data were collected as part of a large study for which the total scan time was limited to 60 min.

Magnetic resonance imaging

Fetal MRI was carried out on a 3.0-T Verio system (Siemens Healthineers, Erlangen, Germany) using a six–channel body-flex array coil, along with a spine coil. A fully flow-compensated 2D/3D-SWI sequence was used to acquire fetal images [12]. The sequence parameters used are given in Table 1. In all subject scans, T2-HASTE and SWI data (2D-SWI or 3D-SWI or both) were acquired multiple times whenever fetal motion was encountered. SWI data were always acquired axial to the fetal brain.

Fetal QSM pipeline and data analysis

Fetal SWI data were first reviewed for general quality, fetal motion, and other artefacts as well as for proper visualisation of the SSS in both magnitude and phase in a series of a minimum of five consecutive images or over 15 mm or 17.5 mm. Thereafter, of the 21 pregnant subjects imaged with 2D-SWI (10), 3D-SWI (9), and both 2D- and 3D-SWI (2), their data were used for QSM processing.

QSM data were generated using the following steps (*see* Fig. 1):

1. The raw phase data were corrected for the global phase offset by forcing the centre phase of k-space to zero.
2. The phase of each image was then subjected to a background field removal method that included the application of homodyne high-pass filtering (16 × 16), followed by a polynomial fitting for remnant low-spatial frequency phase removal.
3. A 3D brain mask was manually extracted from the filtered phase images, ensuring that it included the SSS.
4. The resultant phase data were then used as an input to the iterative, geometry constraint-based thresholded k-space division algorithm [16, 25] to generate QSM. This algorithm takes into account the slab orientation: hence, the orientation of the vein in three dimensions, relative to the B_o axis.
5. QSM images containing the SSS were zoomed twice using a nearest-neighbour interpolation approach and a freehand region of interest (ROI) was drawn inside the SSS. The ROI contained a minimum of 10 voxels.
6. The mean and standard deviation of the $\Delta\chi_v$ distribution inside the SSS were measured from at least two central consecutive slices.
7. To enable comparison to previously published works, $\Delta\chi_{do} = 4\cdot\pi\cdot 0.27$ ppm [30, 31] and the reference Hct values [32] were used in Eq. 3 to quantify the putative S_vO_2 in the SSS.
8. When $\Delta\chi_v$ (and S_vO_2) measurements from multiple SWI volumes were available in a given fetus, the respective values were averaged.
9. The mean and standard error of $\Delta\chi_v$ and S_vO_2 were obtained across all fetuses.

The mean S_vO_2 values obtained were compared to the results from previously published works [10, 12]. Furthermore,

Table 1 2D/3D MRI parameters of a fully flow-compensated SWI sequence

	TR (ms)	TE (ms)	FA (°)	Matrix	Resolution (mm^2)	TH (mm)	No. of slices	BW (Hz/pixel)	Scan time (s)
2D-SWI	280	15–18.7	32	448 × 168–448 × 175	0.78 × 1.56–0.85 × 1.7	3.5	10-11	199	22–24
3D-SWI	23	13.5–17.3	10	448 × 175	0.78 × 1.56	3-3.5	16	219	22–24

TR repetition time, *TE* echo time, *FA* flip angle, *TH* slice thickness, *BW* bandwidth

for each fetal SWI volume where a QSM analysis was performed, the conventional MR susceptometry method was also applied to obtain $S_vO_{2,s}$ as described by Neelavalli et al [10, 12]. QSM-based and susceptometry-based oximetry values were compared using Bland-Altman as a measure of self-consistency in the quantified oxygenation value. A generalised linear model was also used to correlate the two methods. The statistical significance level was set at $p < 0.05$.

Simulations

The spatial extent of phase information in all three directions around the structure of interest is the primary parameter that influences the accuracy of susceptibility values in QSM. Hence, a simulation study using a digital brain phantom [12] was carried out to assess the systematic variability and predict the percentage error in the measured $\Delta\chi_v$ ($\delta\Delta\chi_v$) and the absolute error in fractional S_vO_2 (δS_vO_2) as a function of the mask region around the cross-section of the SSS and as a function of the number of slices (3–7 based on the acquired in vivo data). Simulations were repeated for five different relative orientations of the brain with respect to the B_0: 0°, ± 30° and ± 60°, to account for the variable fetal orientation in utero.

The 3D digital brain phantom used is similar to the one described by Neelavalli et al [12]. The susceptibility values used for the different tissues are listed in Table 2. The brain phantom was first set inside a 1024 × 1024 × 1024 matrix corresponding to an isotropic resolution of 0.2 mm^3 and phase was simulated from this susceptibility matrix using the Fourier-based field perturbation estimation method [27]. The data were then condensed using Fourier cropping to obtain 256 × 256 × 256 matrix with a resolution of 0.8 × 0.8 × 3 mm^3, the same voxel size as that of the in vivo data.

The in-plane mask size around the cross-section of the SSS was varied by factors of 2, 3, 4, 5 and 6 times the SSS diameter

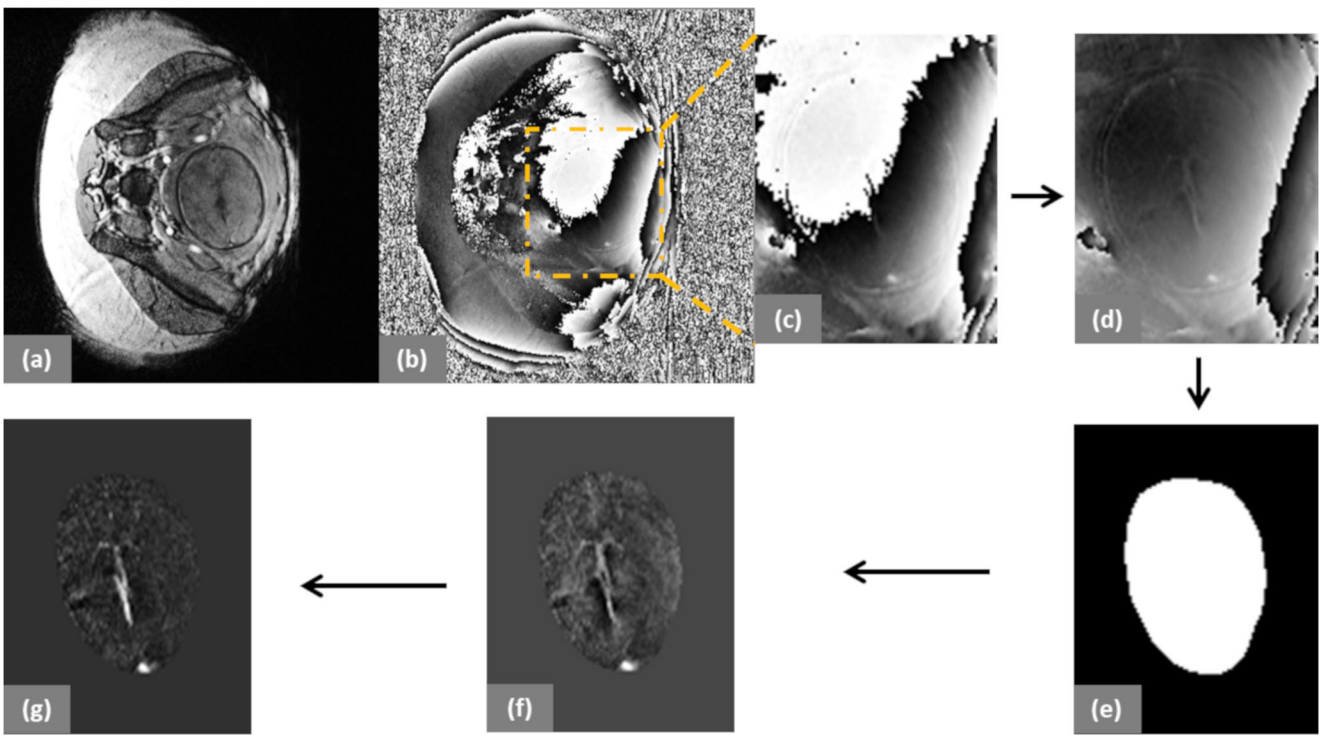

Fig. 1 Representative examples from a fetus at $31^3/_7$ weeks of gestation. **a**, **b** The magnitude and phase images of a fetus inside the maternal abdomen. **c** Cropped raw phase image. **d** Phase-offset corrected phase image. **e** Binary mask of the fetal brain. **f** Phase image after background phase removal using a weak high-pass filter and quadratic fitting. **g** QSM of the fetal brain

Table 2 Brain structures with corresponding magnetic susceptibility values in ppm units are shown. These values are used in the brain model for the simulation

Brain tissue	Magnetic susceptibility (ppm)
Venous vessels	0.45
Grey matter	0.02
White matter	0
Red nucleus	0.13
Substantia nigra	0.16
Crus cerebri	0.03
Thalamus	0.01
Globus pallidus	0.18
Caudate nucleus	0.06
Putamen	0.09
Cerebrospinal fluid	0.014

(i.e. × 2, × 3, × 4, × 5 and × 6, respectively) (Fig. 2). SSS diameter was determined by drawing a circle that exactly encompassed the SSS and then taking its diameter. Circular masks of increasing size (multiples of the vessel diameter) were then generated by fixing one boundary of the circle at the posterior aspect of the SSS and increasing their size in the anterior aspect as shown in Fig. 2. This one-sided region growth was to avoid the fetal skull and the immediate regions outside the fetal head, which often had an unfaithful phase due to large susceptibility differences. An additional 5 voxels between the vessel boundary and the mask boundary on the posterior aspect of the vessel were ensured. This was carried out for five consecutive slices. The masks were asymmetric to accommodate the fact that the extravascular SSS phase is predominantly visible in the immediate brain parenchyma anterior to the vessel. In the posterior aspect of the vessel, phase is not measurable due to the very short T2* of the cranium. Hence, the extent of the mask was limited to 5 voxels in the posterior aspect of the vessel. All the simulations were done using five slices.

In addition, the influence of the number of slices was evaluated by varying the slices containing the vessel, along the long-axis of the vessel, from 3 to 7 (with an increment of one) for the QSM processing. This was assessed at in-plane mask sizes of × 2 (smallest) and × 6 (largest). The $\delta\Delta\chi_v$ and δS_vO_2 were finally assessed with respect to the ground truth value of 0.45 ppm and the corresponding S_vO_2 of 70%, for each simulation.

Results

Simulations

For different sizes of the mask, $\delta\Delta\chi_v$ and δS_vO_2 were less than 3% across all vessel-B_0 orientations (Fig. 3). Error in both $\delta\Delta\chi_v$ and δS_vO_2 increased as the number of slices and the mask size decreased. The δS_vO_2 remained less than 3% ($\delta\Delta\chi_v < 3\%$) for five slices for both extreme masks (× 2 and

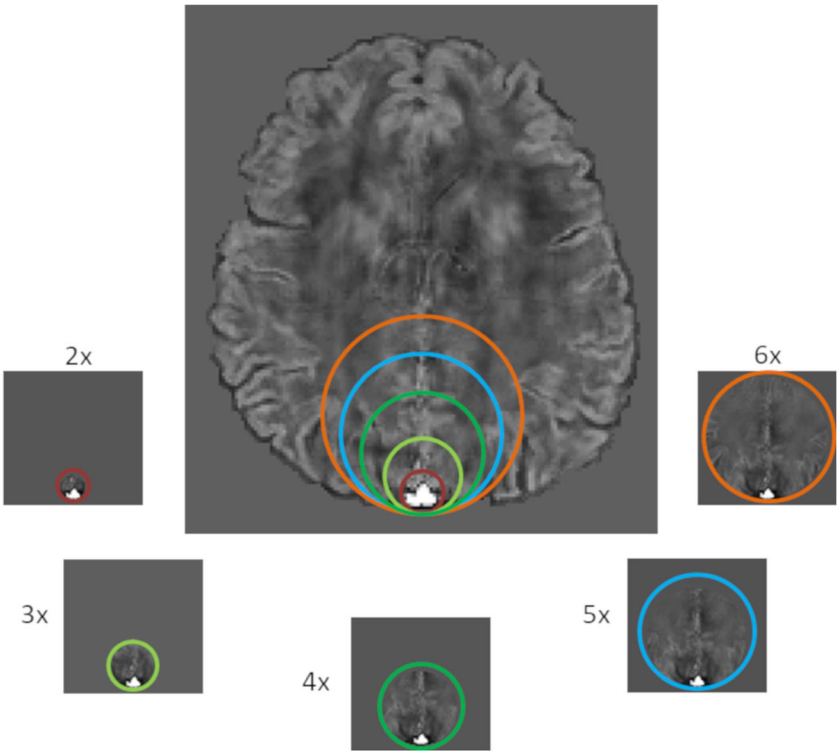

Fig. 2 *Mask generation*: different mask regions labelled × 2, × 3, × 4, × 5 and × 6 as the sizes of SSS are created. The different sizes of the mask regions are *highlighted* with different colours

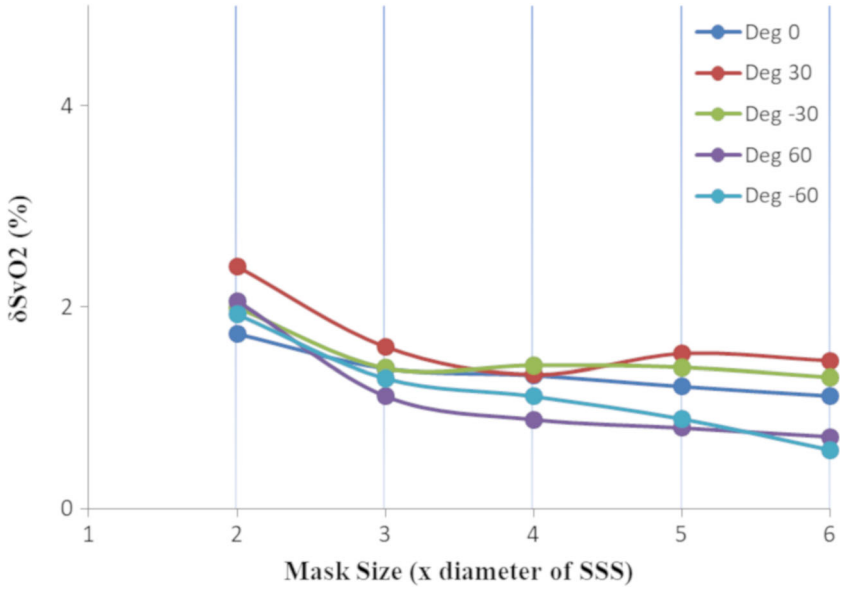

Fig. 3 Relative δS_vO_2 with respect to different mask sizes (relative to the diameters of the SSS) in the QSM of a digital brain is shown. The masks were asymmetric with fixed 5 voxels on the posterior side of the SSS and five slices containing the SSS. The results were obtained for various vessel orientations with respect to B_0. The error was found to be < 3%

× 6), whereas it escalated to 10% ($\delta\Delta\chi_v$ < 11%) and 3% ($\delta\Delta\chi_v$ < 5%) when slices reduced to three for smaller (× 2) and larger (× 6) masks, respectively (Fig. 4). Hence, for fetal QSM processing, at least five consecutive slices were used in all cases.

Fetal QSM

Multiple slices of susceptibility maps of the fetal brain are shown in Fig. 5. The SSS was clearly visible along with evidence of the central sinus. The mean $\Delta\chi_v$ and S_vO_2 in the entire fetal cohort (n = 21) was 0.42 ± 0.03 ppm and 67 ± 7%, respectively. The average $\Delta\chi_v$ and S_vO_2 in second- (n = 5) and third-trimester (n = 16) fetuses were 0.29 ± 0.02 ppm, 75 ± 5%; and 0.47 ± 0.03 ppm, 65 ± 7%, respectively.

QSM-based S_vO_2 and the corresponding susceptometry based $S_vO_{2,\ s}$ measures are shown in Table 3. The Bland-Altman analysis of QSM versus susceptometry-based measures shows very small bias of 0.01% and all the points, except one, lie within the 2-standard deviation range (-4.3 to 4.3) (Fig. 6). This ascertains a strong correlation between the QSM-based $S_vO_2$and the $S_vO_{2,\ s}$ measurements (R^2 = 0.96; $p < 10^{-14}$) for the same volumes of the fetal brain.

Discussion

We demonstrated the feasibility of generating QSM data in human fetuses, which were then used to estimate putative S_vO_2 in the SSS. The average S_vO_2 obtained is in close agreement with the values found in the fetal literature [12, 33, 34]. A $\Delta\chi_{do}$ value for adult blood (0.27 ppm [25]) was used in estimating the S_vO_2 so that comparison to previously published susceptometry literature could be performed. A recent work [35] has shown that for third-trimester fetuses the $\Delta\chi_{do}$ value is 0.21 ppm. If we use this value, the average S_vO_2 value

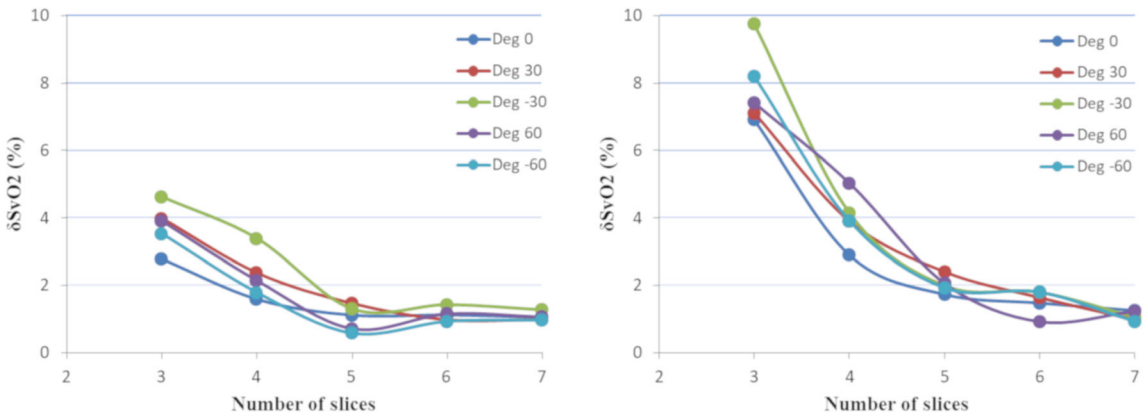

Fig. 4 Relative δS_vO_2 with respect to the different number of slices (3–7) used in the QSM of a digital brain phantom for (*left*) mask size 6 times larger than SSS and (*right*) mask size 2 times larger than SSS, are shown. The δS_vO_2 decreases as the number of slices increases, which is < 3% for five slices for both the mask sizes and < 5% ($\delta\chi_v$ < 6%) and < 10% ($\delta\chi_v$ < 11%) for three slices for larger and smaller mask sizes, respectively

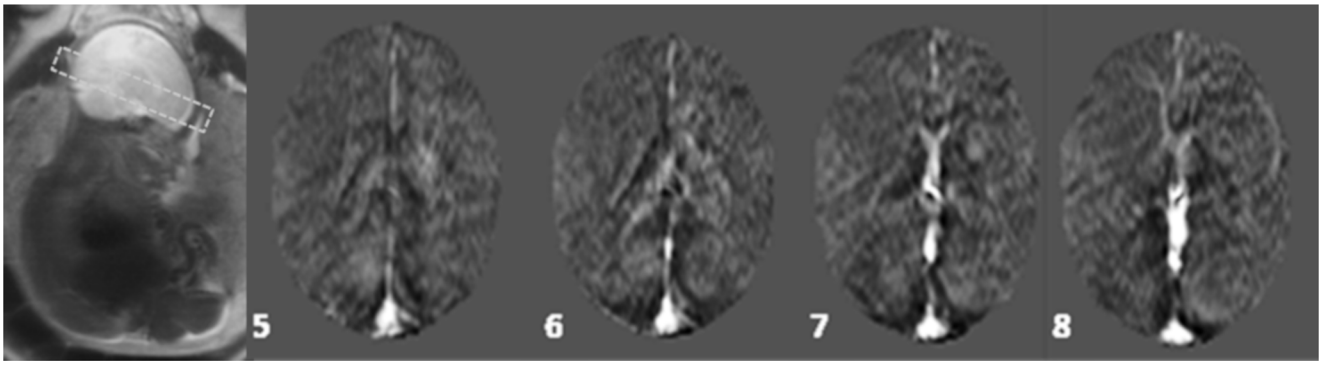

Fig. 5 A collage of multiple slices (as numbered) showing the susceptibility maps of a fetal brain. Major vessels such as SSS, straight sinus, and transverse sinus can be seen along with small veins near the corpus callosum. GA: 29 weeks

would drop to 55%. However, this baseline shift in S_vO_2 will not affect the conclusion of our feasibility study.

The QSM pipeline was adopted from the general adult QSM processing with some modifications. In the adult brain, commonly the Brain Extraction Tool (BET) [36] is used to generate binary masks of the brain-only region. However, due to factors such as the arbitrary orientation of the fetal brain, susceptibility artefacts from the close proximity of the gas-filled intestine and pubic/lumbar spinal bone, and presence of high-intensity regions, e.g. the maternal bladder, using BET for brain extraction was not possible. To overcome this issue, we manual segmented out the fetal brain from the filtered phase images and excluded any regions corrupted by major artefacts. The mask was chosen such that the phase information around the SSS was preserved. Since the SSS lies on the posterior edge of the fetal brain, it was challenging to obtain a large symmetric region around the vessel due to the artefacts coming from the maternal organs. Therefore, we used an asymmetric region around the SSS (*see* Fig. 1). Results from simulations provided an indication of the systematic errors that could be expected in the QSM processing due to the limited number of voxels around the SSS and the number of slices covering the SSS. The external phase behaviour for a vein decays at a rate of $\frac{1}{(radius)^2}$. Hence, the most dominant phase information required to reconstruct the susceptibility maps is present in the pixels nearest to the vein boundary. This was confirmed when we observed that δS_vO_2 in the SSS remains less than 3%, provided the mask size, in the plane of the cross-section of the vessel, is twice the size of the diameter of the vessel and the vessel is contained in five slices. Results from the simulation study affirmed the reliability of the optimised pipeline for the fetal QSM used in this work.

Table 3 The venous blood oxygenation values estimated using the QSM-based and MR susceptometry-based techniques

Gestational age (weeks)	Oxygenation using susceptometry (%)	Oxygenation using QSM (%)
35.3	56.0 ± 1.8	56.2 ± 6.7
21	86.2 ± 2.0	86.6 ± 4.4
34.1	65.2 ± 1.2	64.9 ± 9.5
23.7	84.5 ± 1.2	82.1 ± 2.2
31.3	75.9 ± 1.9	73.2 ± 5.9
24	68.8 ± 1.8	65.5 ± 7.0
27.1	62.5 ± 3.1	65.7 ± 4.8
28.9	60.1 ± 1.8	65.6 ± 5.7
37.4	57.4 ± 1.2	57.2 ± 4.9
31.9	56.4 ± 1.0	57.4 ± 5.9
35.7	68.5 ± 2.1	66.2 ± 4.6
29	61.0 ± 1.3	61.8 ± 6.9
20.7	67.9 ± 3.2	67.5 ± 4.5
36.4	44.2 ± 2.8	45.0 ± 6.9
37	63.7 ± 2.0	66.8 ± 6.2
36.6	80.0 ± 6.7	81.6 ± 10.3
27.9	82.6 ± 2.8	81.9 ± 6.0
29	80.5 ± 1.5	79.8 ± 4.8
26.3	80.7 ± 1.8	79.6 ± 5.9
31.4	63.5 ± 4.0	64.1 ± 11.8
33.9	74.2 ± 1.9	71.2 ± 3.8

To remove the background phase, we used a 16 × 16 homodyne filter, followed by a quadratic fitting for edge preservation. The high-pass filter causes some level of phase signal loss depending on the size of the object [23]. However, a 16 × 16 homodyne filter with an in-plane matrix of 448 × 448 and a resolution of 0.8mm is equivalent to a filter that will affect structures of 35 pixels (28 mm) in size or greater. Therefore, irrespective of the vessel orientation, the use of a small filter of 16 × 16 leads to minimal loss of local phase of the fetal SSS whose maximum diameter is 4–8 mm at term [37].

Fetal SWI sequence used in this study was flow-compensated in all the three directions and hence, S_vO_2 estimation in SSS was not affected by the blood flow. The QSM-based S_vO_2 was highly correlated with the $S_vO_{2,s}$ measured from the same volumes. MR susceptometry method uses intravascular phase to estimate $S_vO_{2,s}$ which is dependent on the curvature and orientation of the blood vessel. It assumes the

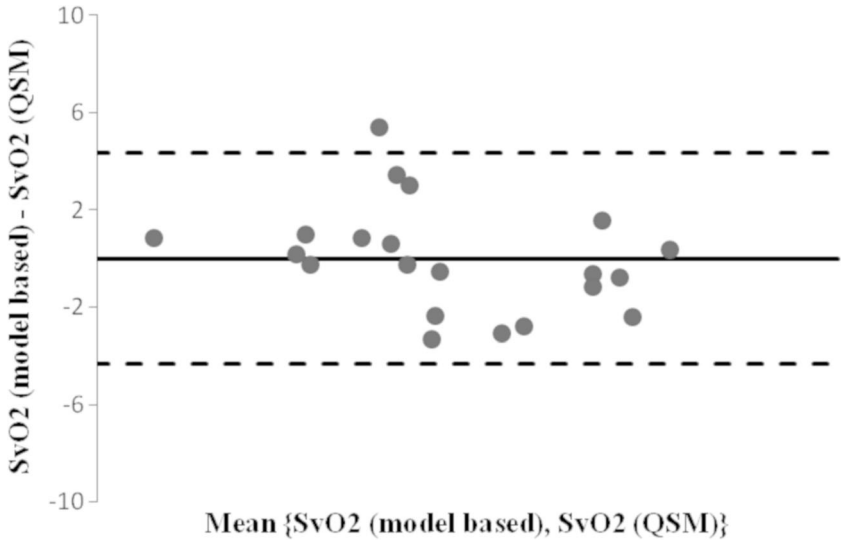

Fig. 6 The Bland-Altman plot (oxygenation difference vs mean oxygenation of model-based and QSM-based methods) shows a small bias of 0.01% and all points, but one, lie within the 2-standard deviation range. This ascertains a strong correlation between the two measurements $R^2 = 0.96$; $p < 10^{-14}$

blood vessel to be a long cylinder. Although the straight section of the SSS was chosen for susceptometry, error may be present in $S_vO_{2,\,s}$ due to a small error in the vessel angle and non-circular cross-section of the SSS. Compared to MR susceptometry, QSM does not rely on orientation and geometry-based assumptions. Nevertheless, we found no statistical difference between the two techniques, which ascertains our results of accurate phase measurement using cylindrical approximation and confirms the accuracy and reproducibility of QSM measurements.

While the focus of our paper is the application of QSM technique to fetal blood oximetry, we observe that in our small sample size, the measured S_vO_2 values in the second trimester group are higher than that in the third trimester group. This is consistent with the trend that was reported recently [10] and with that seen in previous in vivo studies, where the blood oxygenation (both pO2 and SO2) in umbilical venous blood samples, was found to decrease with advancing gestational age [38–40]. Furthermore, it is also known that the cerebral blood flow rate to the human fetal brain increases from second to third trimester [41]. Taken together, the flow and oxygen saturation changes may be towards accommodating the increased metabolic demand that is seen during the third trimester.

There are some shortcomings in this study. First, the mask generation using manual intervention is time-consuming. We created a mask of all the slices containing the SSS in all the fetal data. An automated fetal BET would be very helpful in the future [42]. Second, for the simulations, we used a digital phantom that has features of the adult brain, which has less curvature in the SSS vessel than in the fetus. Nevertheless, we used the same spatial resolution as in our fetal data and chose slices from the curved region of the SSS in the simulations. This model provided a reasonable representation of the fetal brain. In addition, the cross-section of SSS is an approximate triangle that might affect the precise formation of the mask sizes as a factor of SSS size. However, we tried to standardise our mask creation process by only moving the anterior point upwards to achieve different mask sizes. Third, we used longer TE in this study to achieve a good phase signal-to-noise ratio (SNR) in SWI. A shorter TE could be more useful in QSM processing due to less T2* signal loss and phase aliasing inside and at the boundaries of the veins. In addition, it could also help reduce the imaging time without sacrificing the phase SNR.

Conclusions

This study demonstrates the feasibility of using QSM in human fetuses. The putative S_vO_2 of 67 ± 7% obtained from the $\Delta\chi_v$ maps was in close agreement with previously published fetal literature.

Acknowledgements Dr. Romero has contributed to this work as part of his official duties as an employee of the United States Federal Government.

Funding This research was supported, in part, by the Perinatology Research Branch (PRB), Program for Perinatal Research and Obstetrics, Division of Intramural Research, Eunice Kennedy Shriver National Institute of Child Health and Human Development, National Institutes of Health, U.S. Department of Health and Human Services (NICHD/NIH/DHHS); in part, with Federal funds from NICHD/NIH/DHHS under Contract No. HHSN275201300006C; and an STTR grant from the NHLBI number 1R42HL112580- 01A1.

Compliance with ethical standards

Guarantor The scientific guarantor of this publication is Dr. Jaladhar Neelavalli.

Conflict of interest The authors of this manuscript declare no relationships with any companies, whose products or services may be related to the subject matter of the article.

Statistics and biometry No complex statistical methods were necessary for this paper.

Informed consent Written informed consent was obtained from all subjects (patients) in this study.

Ethical approval Institutional review board approval was obtained.

Study subjects or cohorts overlap The imaging data used in this manuscript has been used in part previously in an earlier manuscript (Yadav et al [10]), which evaluated fetal blood oxygenation as a function of gestational age in a larger cohort. This manuscript, on the other hand, focuses on demonstrating the applicability of a novel technique in the human fetus for in vivo blood oximetry and compares the results with those obtained using the standard model-dependent method. We find that the results affirm the applicability of both methods for in vivo fetal blood susceptometry and oximetry.

Methodology
- Prospective
- Experimental
- Performed at one institution

References

1. Schneider H (2011) Oxygenation of the placental–fetal unit in humans. Respir Physiol Neurobiol 178:51-58
2. Gagnon R (2003) Placental insufficiency and its consequences. Eur J Obstet Gynecol Reprod Biol 110:S99–S107
3. Maberry MC, Ramin SM, Gilstrap LC 3rd, Leveno KJ, Dax JS (1990) Intrapartum asphyxia in pregnancies complicated by intraamniotic infection. Obstet Gynecol 76:351–354
4. Escobar J, Teramo K, Stefanovic V et al (2013) Amniotic fluid oxidative and nitrosative stress biomarkers correlate with fetal chronic hypoxia in diabetic pregnancies. Neonatology 103:193–198
5. Low JA, Galbraith RS, Muir DW, Killen HL, Pater EA, Karchmar EJ (1985) The relationship between perinatal hypoxia and newborn encephalopathy. Am J Obstet Gynecol 152:256–260
6. Gunn AJ, Bennet L (2009) Fetal hypoxia insults and patterns of brain injury: insights from animal models. Clin Perinatol 36:579–593
7. Hall D (1989) Birth asphyxia and cerebral palsy. BMJ 299(6694): 279
8. Cetin I, Barberis B, Brusati V et al (2011) Lactate detection in the brain of growth-restricted fetuses with magnetic resonance spectroscopy. Am J Obstet Gynecol 205:350.e1–350.e7
9. Krishnamurthy U, Yadav BK, Jella PK et al (2018) Quantitative flow imaging in human umbilical vessels in utero using nongated 2d phase contrast MRI. J Magn Reson Imaging 48:283–289
10. Yadav BK, Krishnamurthy U, Buch S et al (2018) Imaging putative foetal cerebral blood oxygenation using susceptibility weighted imaging (SWI). Eur Radiol (28):1884–1890
11. Zhu MY, Milligan N, Keating S et al (2016) The hemodynamics of late-onset intrauterine growth restriction by MRI. Am J Obstet Gynecol 214:367.e1–367.e17
12. Neelavalli J, Jella PK, Krishnamurthy U et al (2014) Measuring venous blood oxygenation in fetal brain using susceptibility-weighted imaging. J Magn Reson Imaging 39:998–1006
13. Stuber M, Botnar RM, Fischer SE et al (2002) Preliminary report on in vivo coronary MRA at 3 Tesla in humans. Magn Reson Med 48: 425–429
14. Neelavalli J, Mody S, Yeo L et al (2014) MR venography of the fetal brain using susceptibility weighted imaging. J Magn Reson Imaging 40:949–957
15. Haacke EM, Liu S, Buch S, Zheng W, Wu D, Ye Y (2015) Quantitative susceptibility mapping: current status and future directions. Magn Reson Med 33(1):–25
16. Haacke EM, Tang J, Neelavalli J, Cheng YC (2010) Susceptibility mapping as a means to visualize veins and quantify oxygen saturation. J Magn Reson Imaging 32:663-676
17. Liu T, Surapaneni K, Lou M, Cheng L, Spincemaille P, Wang Y (2012) Cerebral microbleeds: burden assessment by using quantitative susceptibility mapping. Radiology 262:269–278
18. Deistung A, Schweser F, Reichenbach JR (2017) Overview of quantitative susceptibility mapping. NMR Biomed 30(4):e3569
19. Liu C, Wei H, Gong NJ, Cronin M, Dibb R, Decker K (2015) Quantitative susceptibility mapping: contrast mechanisms and clinical applications. Tomography 1(1):3
20. Liu C, Li W, Tong KA, Yeom KW, Kuzminski S (2015) Susceptibility-weighted imaging and quantitative susceptibility mapping in the brain. J Magn Reson Imaging 42:23–41
21. Carpenter KL, Li W, Wei H et al (2016) Magnetic susceptibility of brain iron is associated with childhood spatial IQ. Neuroimage 132: 167–174
22. Liu J, Xia S, Hanks R et al (2016) Susceptibility weighted imaging and mapping of micro-hemorrhages and major deep veins after traumatic brain injury. J Neurotrauma 33:10–21
23. Haacke EM, Reichenbach JR (2014) Susceptibility weighted imaging in MRI: basic concepts and clinical applications. Wiley-Blackwell, Hoboken
24. Weisskoff RM, Kiihne S (1992) MRI susceptometry: image-based measurement of absolute susceptibility of MR contrast agents and human blood. Magn Reson Med 24:375–383
25. Tang J, Liu S, Neelavalli J, Cheng YC, Buch S, Haacke EM (2013) Improving susceptibility mapping using a threshold-based K-space/image domain iterative reconstruction approach. Magn Reson Med 69:1396–1407
26. de Rochefort L, Brown R, Prince MR, Wang Y (2008) Quantitative MR susceptibility mapping using piece-wise constant regularized inversion of the magnetic field. Magn Reson Med 60:1003–1009
27. Wharton S, Schäfer A, Bowtell R (2010) Susceptibility mapping in the human brain using threshold-based k-space division. Magn Reson Med 63:1292–1304
28. Schweser F, Deistung A, Lehr BW, Reichenbach JR (2010) Differentiation between diamagnetic and paramagnetic cerebral lesions based on magnetic susceptibility mapping. Med Phys 37: 5165–5178
29. Neelavalli J, Cheng YC, Haacke M (2005) Method for susceptibility calculation in multiple source object distribution with arbitrary susceptibilities: a preliminary report. No. 2333, Proceedings of the International Society for Magnetic Resonance in Medicine, Miami Beach Convention Center, Miami, 7–13 May 2005
30. Spees WM, Yablonskiy DA, Oswood MC, Ackerman JJ (2001) Water proton MR properties of human blood at 1.5 Tesla: magnetic susceptibility, T1, T2, T* 2, and non-Lorentzian signal behavior. Magn Reson Med 45:533–542
31. Jain V, Abdulmalik O, Propert KJ, Wehrli FW (2012) Investigating the magnetic susceptibility properties of fresh human blood for noninvasive oxygen saturation quantification. Magn Reson Med 68:863–867

32. Boulot P, Cattaneo A, Taib J et al (1993) Hematologic values of fetal blood obtained by means of cordocentesis. Fetal Ther 8:309–316
33. Chua S, Yeong S, Razvi K, Arulkumaran S (1997) Fetal oxygen saturation during labour. Br J Obstet Gynaecol 104:1080–1083
34. Dildy GA, Thorp JA, Yeast JD, Clark SL (1996) The relationship between oxygen saturation and pH in umbilical blood: implications for intrapartum fetal oxygen saturation monitoring. Am J Obstet Gynecol 175(3 Pt 1):682–687
35. Portnoy S, Milligan N, Seed M, Sled JG, Macgowan CK (2018) Human umbilical cord blood relaxation times and susceptibility at 3 T. Magn Reson Med 79:3194–3206
36. Smith SM (2002) Fast robust automated brain extraction. Hum Brain Mapp 17:143–155
37. Pooh RK, Kurjak A (2010) Fetal brain vascularity visualized by conventional 2D and 3D power Doppler technology. DSJUOG 4: 249–258
38. Soothill PW, Nicolaides KH, Rodeck CH, Campbell S (1986) Effect of gestational age on fetal and intervillous blood gas and acid-base values in human pregnancy. Fetal Ther 1:168–175
39. Nicolaides KH, Economides DL, Soothill PW (1989) Blood gases, pH, and lactate in appropriate-and small-for-gestational-age fetuses. Am J Obstet Gynecol 161:996–1001
40. Schröter B, Chaoui R, Glatzel E, Bollmann R (1997) [Normal value curves for intrauterine fetal blood gas and acid-base parameters in the 2nd and 3rd trimester]. Gynakol Geburtshilfliche Rundsch 37: 130–135
41. Veille JC, Hanson R, Tatum K (1993) Longitudinal quantitation of middle cerebral artery blood flow in normal human fetuses. Am J Obstet Gynecol 169:1393–1398
42. Habas PA, Kim K, Corbett-Detig JM et al (2010) A spatiotemporal atlas of MR intensity, tissue probability and shape of the fetal brain with application to segmentation. Neuroimage 53:460–470